ACS APPLIED MATERIALS & INTERFACES

Research Article

www.acsami.org

A Versatile Strategy toward Binary Three-Dimensional Architectures Based on Engineering Graphene Aerogels with Porous Carbon Fabrics for Supercapacitors

Wei-Li Song,[†] Kuo Song,[†] and Li-Zhen Fan*,[†]

[†]Institute of Advanced Materials and Technology, University of Science and Technology Beijing, Beijing, 100083, P. R. China

Supporting Information

ABSTRACT: Graphene-based supercapacitors and related flexible devices have attracted great attention because of the increasing demands in the energy storage. As promising three-dimensional (3D) nanostructures in the supercapacitor electrodes, graphene-based aerogels have been paid dramatic attention recently, and numerous methods have been developed for enhancing their performance in energy storage. In this study, an exclusive strategy is presented toward directly in situ growing reduced graphene oxide (RGO) aerogels inside the 3D porous carbon fabrics for engineering the interfaces of the resulting binary 3D architectures. Such unique architectures have shown various advantages in the improvements of the nanostructures and chemical compositions, allowing them to possess much enhanced electrochemical properties (391, 229, and 195 F g^{-1} at current densities of 0.1, 1, and 5 A g^{-1}, respectively) with excellent cycling stability in comparison with the neat RGO aerogels. The results of the performance in the flexible all-solid-state supercapacitors along with discussion on the related mechanisms in the electrochemical properties indicate the remaining issues and associated opportunities in the development of advanced energy storage devices. This strategy is relatively facile, versatile, and tunable, which highlights a unique platform for engineering various 3D porous structures in many fields.

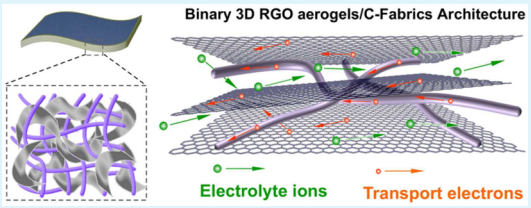

KEYWORDS: *3D architecture, supercapacitors, aerogels, porous nanostructures, energy storage*

INTRODUCTION

The dramatic development of portable electronic devices and hybrid electric vehicles has created a large demand for innovative energy storage materials of high power density and efficient energy conversion.[1−6] Owing to the high power density, long cycle life, and fast charge/discharge processes, electrochemical supercapacitors enable rapid energy recovery in heavier duty systems, and they are recently required to be lightweight, flexible, and effective for meeting the urgent requirement in the industry.[7−9] Carbon-based materials of porous structures have been mostly considered as the ideal electrodes for electrical double-layer capacitors (EDLCs).[1−3] Particularly, efforts have been dedicated to exploring porous three-dimensional (3D) carbon-based nanostructures currently due to their advantageous features of enhanced ion and electron transport and high specific capacities as well as their superior electrochemical stability.[10−12]

For the unique porous 3D frameworks, graphene-based foams, hydrogels, and aerogels have attracted increasing interest in the community.[13−21] A remarkable variety of explorative studies have been reported for achieving such lightweight porous 3D graphene nanostructures, suggesting excellent specific capacitance and cycling stability.[13,14,16,18−21] As a typical example, Duan and co-workers have fabricated flexible all-solid-state supercapacitors based on reduced graphene oxide (RGO) hydrogels, demonstrating enhanced specific capacitance up to 186 F g^{-1} with area specific capacitance of 372 F cm^{-2} (current density of 1 A g^{-1}) in a two-electrode poly(vinyl alcohol) (PVA)/H_2SO_4 gel system.[16] Generally speaking, the utilization of freeze-drying has been well-known to be an effective method for considerably preventing RGO nanosheets from restacking and aggregation in the formation of 3D graphene-based nanostructures. On the basis of this strategy, recent efforts have suggested that significant improvements could be achieved by further engineering the interfaces or chemical compositions of the graphene-based nanostructures, including doping with heteroatoms,[22−24] introduction of a heterocompound as the spacers,[25−27] generation of unique ionic channels,[8] etc. Among these approaches, the attempt of utilizing metal oxides as the spacers to synthesize 3D graphene/metal oxide hybrid structures presents several shortages in the decreased rate performance and poor cycling stability induced by the transition metal oxides.[28] On the contrary, carbonaceous materials, such as carbon black,[26] carbon nanotubes,[24,29,30] and highly ordered porous carbon particles,[27] have been reported to be the effective spacers for enhancing the related energy storage performance via the optimization of the porous structures, specific surface areas, and interfaces of the resulting 3D graphene-based nanostructures.

Received: December 7, 2014
Accepted: February 5, 2015
Published: February 5, 2015

DOI: 10.1021/am508624x
ACS Appl. Mater. Interfaces 2015, 7, 4257−4264

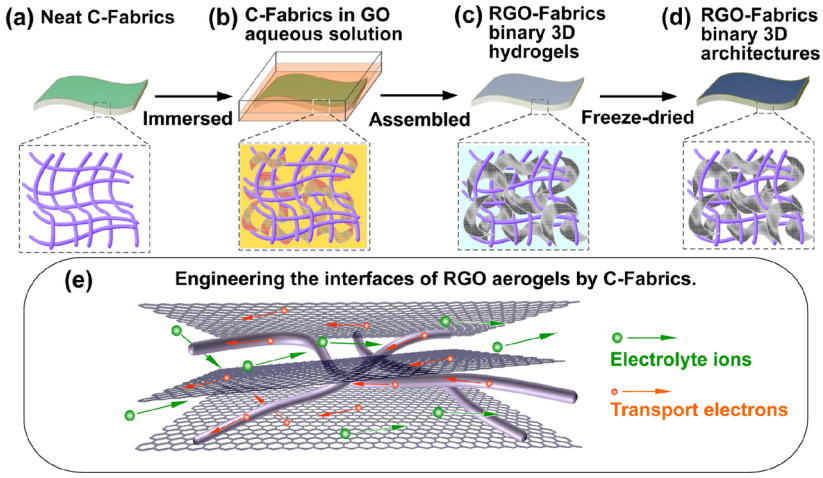

Figure 1. (a–d) Fabrication of the binary 3D architectures. (e) Engineering the interfaces of RGO aerogels with C-fabrics, showing effective charge diffusion and transfer in the binary 3D architectures (graphene motifs not drawn to scale).

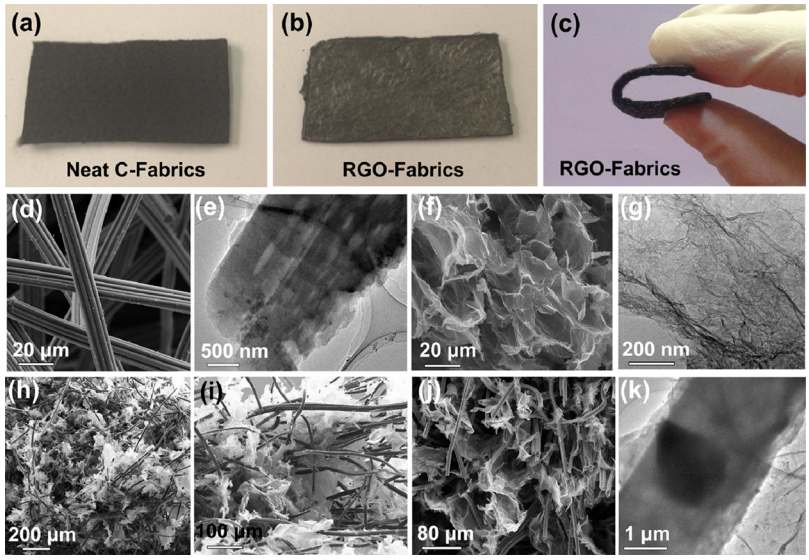

Figure 2. Optical photos of the neat C-fabrics (a), RGO fabrics (b), and flexible RGO fabrics upon bending (c); SEM image (d) and TEM image (e) of the neat C-fabrics; SEM image (f) and TEM image (g) of the neat RGO aerogels; SEM images (h–j) and TEM image (k) of the RGO fabrics.

On the other hand, typical continuous 3D carbon frameworks, including carbon cloths, textures, and fabrics, have also received extensive attention because of their advantages, such as intrinsic electrically conductive networks for electronic transport and porous structures for efficient ionic diffusion.[31−36] As a consequence, they have been widely used as the matrices/substrates for preparing hybrid structures, aiming to achieve high-performance energy-storage devices.[31−36] For example, Yang et al. have synthesized MnO_2 nanowires and Fe_2O_3 nanotubes on the carbon fabrics separately and further processed them into solid-state asymmetric supercapacitors, with extended operating voltage window and high energy density observed.[31] Similarly, a hierarchical $NiCo_2O_4$@NiO core–shell nanowire heteronanostructure has been grown on the carbon cloths,[36] and the fabricated flexible solid-state supercapacitors exhibited an enhanced capacitance with the capacity retention of 87.5% after 5000 cycles.

In the present work, we demonstrate a simple and versatile strategy for processing 3D porous carbon fabrics (surface area $\approx$ 1111 m^2 g^{-1}) into 3D RGO aerogels to fabricate a novel binary 3D architecture, with the purpose of engineering the interface, nanostructure, and electrochemical performance of RGO aerogels. Compared to the neat RGO aerogels without using carbon fabrics, the as-fabricated RGO aerogel/carbon fabrics (RGO fabrics) of binary 3D architectures were found to present much increased specific surface area with increased micropores, improved networks, and channels for electronic transport and ionic diffusion. Thus, they were able to deliver an enhanced specific capacitance (391, 229, and 195 F g^{-1} at current densities of 0.1, 1, and 5 A g^{-1}, respectively) and excellent cycling stability. The highest capacitance, up to 245 F g^{-1} at 0.1 A g^{-1}, along with good capacitive retention was also found in the related fabricated flexible all-solid-state supercapacitors. Some remaining issues and associated opportunities based on such facile technique are discussed.

RESULTS AND DISCUSSION

In the fabrication of the binary 3D architectures, a piece of acid-treated C-fabrics (~2 mm in thickness) was immersed in the GO aqueous solution (Figure 1a,b), followed by adding hydroquinone as the reducing agent. Until the stable GO–hydroquinone solution was homogeneously dispersed in the C-

DOI: 10.1021/am508624x
ACS Appl. Mater. Interfaces 2015, 7, 4257–4264

fabric skeleton, the mixtures were sealed and transferred into an oven for the in situ establishment of 3D RGO frameworks via combination of hydrophobic and $\pi-\pi$ interactions during the reduction of GO (Figure 1c).[27,37] The resulting hydrogel-like products were further freeze-dried and thermally annealed to achieve the RGO fabrics (Figure 1d).

In the exclusive strategy for designing such novel binary 3D architectures, it is noteworthy that utilization of the porous C-fabrics for engineering the interface, nanostructure, and electrochemical performance of RGO aerogels show several unique advantageous features. (1) Immersion of C-fabrics in the GO solution enables the GO nanosheets to be homogeneously dispersed in the interspaces of the C-fabric skeleton, by which RGO aerogels could be in situ generated in the C-fabrics. (2) The mechanical brittleness of the RGO aerogels could be substantially improved by the introduced C-fabric skeleton, allowing the resultant RGO fabrics to be highly mechanically flexible and robust. (3) The presence of the C-fabric skeleton could well alleviate the volume shrinkage and unexpected restacking upon the in situ formation of RGO aerogels, with anticipation of significantly improving the interfaces and ionic channels of the 3D RGO aerogels. (4) The introduced porous C-fabrics of high surface area and sufficient micropores are expected to essentially enhance the energy storage via synergy effects in the binary 3D architectures (Figure 1e).

As shown in the optical photos (Figure 2a,b), the shape of the resulting RGO fabrics was mainly determined by the dimension of the introduced C-fabrics, and the RGO aerogels were in situ formed inside the C-fabrics. Because of the 3D skeleton of the C-fabrics, the RGO fabrics were found to be mechanically robust and highly flexible (Figure 2c). Figure 2d exhibits the scanning electron microscopy (SEM) image of the neat C-fabrics used for engineering the RGO aerogels, which demonstrate the typical continuous 3D skeletons formed by carbon fibers. Representative transmission electron microscopy (TEM) image displays the porous feature of the ground short C-fabrics (Figure 2e). According to SEM and TEM images in Figure 2f,g, respectively, the neat RGO aerogels without the presence of C-fabrics demonstrate highly porous structures, with wrinkled RGO nanosheets in the as-formed 3D frameworks. For the RGO fabrics, Figure 2h (~1 mm scale) and Figure 2i shows the representative cross-section views for the binary 3D architectures, suggesting that continuous 3D RGO frameworks were expected to be homogeneously generated in the entire 3D C-fabric skeleton. Figure 2j and Supporting Information, Figure S1 clearly show that the introduced 3D C-fabric skeleton has effectively prevented the RGO frameworks from unexpected aggregation/restacking and volume shrinkage during the formation of aerogels and post-treatments. Therefore, the interfaces of the RGO fabrics have been greatly improved via the establishment of the binary 3D architectures, compared to those of the neat RGO aerogel and neat C-fabrics. TEM image in Figure 2k briefly exhibits the overlap of the ground short C-fabrics on a piece of RGO nanosheet.

X-ray photoelectron spectroscopy (XPS) was carried out to investigate the chemical compositions of the samples. As shown in Figure 3a, all the samples present sharp C peaks, and corresponding concentrations of C, O, and N elements were listed in Supporting Information, Table S1. The neat C-fabrics, neat RGO aerogels, and RGO fabrics possess C concentrations of 87.9%, 84.89%, and 85.62%, respectively. Figure 3b–d exhibits the C 1s spectra, indicating dominant carbon–carbon

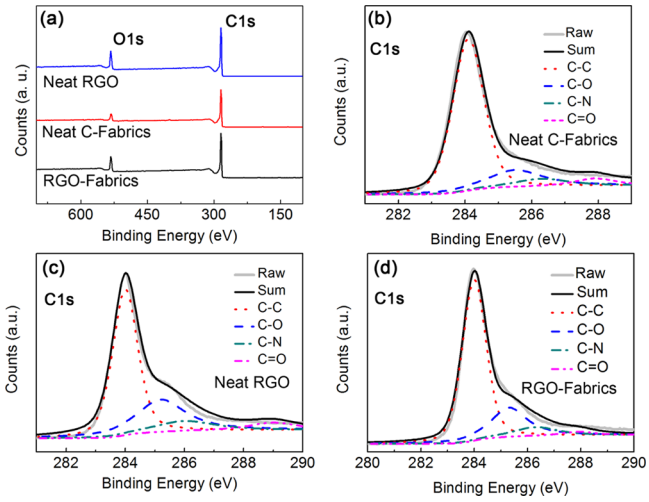

Figure 3. XPS spectra for the samples as marked (a), C 1s spectra of the neat C-fabrics (b), neat RGO (c), and RGO fabrics (d).

species (~284.6 eV) in all the three samples.[38] Compared to the neat C-fabrics, RGO fabrics presented slightly increased C–O (~286.1 eV) species due to the presence of RGO aerogels as expected (Table S1). Such species, which refer to oxygen-containing functional groups (carboxyl and hydroxyl groups as examples), mainly contribute to the increase of specific capacitance via pseudocapacitive interactions.[6,39,40] Moreover, observation in Supporting Information, Figure S1 suggests that the connection between RGO aerogel and C-fabrics is mainly associated with the generation of hydrogen bonding due to the presence of carboxyl groups along with hydroxyl groups in both GO and C-fabrics. Compared to the neat RGO, on the other hand, increased amount of N element observed in the RGO fabrics was mainly due to the N element in the introduced C-fabrics (Table S1). Accordingly, different types of nitrogen-containing functional groups in the neat C-fabrics and RGO fabrics indicate that the dominant peaks at 400.6 and 398.1 eV are associated with quaternary N (N-Q) and pyridine (N-6) species, respectively (Supporting Information, Figure S2).[6,41,42] In general, the presence of increased positively charged N-Q could improve the electron transfer in the electrode.[6,41,42] Therefore, the XPS results suggest that the binary 3D architectures may hold the advantages of both oxygen- and nitrogen-containing functional groups from the RGO aerogels and C-fabrics, respectively, which may contribute to improved electrochemical performance. Further Raman characterizations suggest typical broad G-band (~1585 cm^{-1}) and D-band (~1350 cm^{-1}) in the RGO fabrics, which indicate the features from both neat RGO aerogel and neat C-fabrics as expected (Supporting Information, Figure S3).

The nitrogen adsorption–desorption isotherms of the three samples are exhibited in Figure 4a. The total surface area (S_{total}) and surface area of micropores (S_{micro}) were calculated from multipoint Brumauer–Emmett–Teller (BET) plot and $V-t$ plot, respectively. Surface area of mesopore and macropore ($S_{meso+macro}$) was obtained by subtracting S_{micro} from S_{total}. Total pore volume (V_{total}) was determined at P/P_0 = 0.99, and micropore volume (V_{micro}) was obtained from $V-t$ plot (Supporting Information, Table S2). According to Figure 4a, it is clear to observe strong adsorption below the relative pressure of P/P_0 = 0.1 in the RGO fabrics, consistent with the observation in the neat C-fabrics, which suggests a feature of

DOI: 10.1021/am508624x
ACS Appl. Mater. Interfaces 2015, 7, 4257–4264

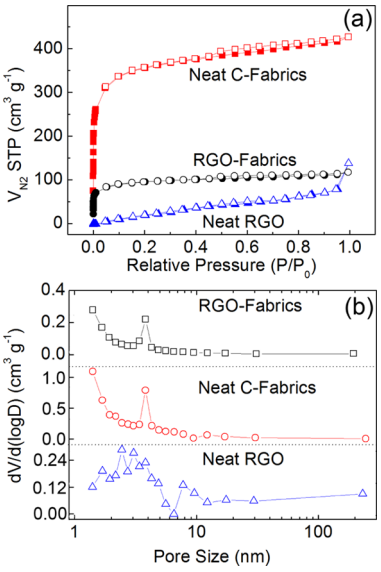

Figure 4. N_2 adsorption−desorption isotherms of the samples as marked. (a) Pore size distribution of the samples as marked (b).

micropore filling.[43,44] In the relative pressure range of 0.1−0.5 along with gradually decreased slope above 0.5, both the RGO fabrics and neat C-fabrics present a typical IV isotherm with the hysteresis loop feature of mesopores. In the relative pressure range of $P/P_0 > 0.9$, a tail was found in the isotherm of the RGO fabrics, which is consistent with a sharp nitrogen uptake in the neat RGO aerogels (Figure 4a), suggesting a feature of macropores.[44] Accordingly, the surface area of micropores was calculated to be 287.3 $m^2 g^{-1}$ out of 322.6 $m^2 g^{-1}$ (total surface area) in the RGO fabrics (Table S2), indicating a significant increase in comparison with that in the neat RGO (total surface area ≈ 174.4 $m^2 g^{-1}$). The observation suggests that the RGO fabrics (15 wt % RGO) present smaller specific surface area than the neat C-fabrics, which is mainly associated with the changes of the carbon configurations and nanostructures in the C-fabrics upon the acid treatment, subsequent reduction, and thermal annealing processes.[39] As shown in Figure 4b, the pore size distribution was calculated from density functional theory. Although RGO fabrics demonstrate a peak at ∼4 nm (Figure 4b), the estimated average pore size was calculated to be 2.253 nm, due to the major feature of micropores (<2 nm). This value is similar to that of the neat C-fabrics (2.37 nm), which is also in the majority of micropores, but different from that of the neat RGO aerogel (4.88 nm) as expected. Consequently, the results here indicate that the employment of C-fabrics in the RGO aerogels has substantially increased the surface area via preventing RGO restacking in the formation of aerogels as well as increasing the micropores.

Apart from the observation in the interface improvement via generating the binary 3D frameworks, combined results of XPS and nitrogen adsorption−desorption analysis further imply that the resulting RGO fabrics of unique porous nanostructures and chemical compositions are expected to deliver enhanced electrochemical properties in the corresponding energy-storage devices.

For the electrochemical measurements, the samples were fabricated into the electrodes, followed by being assembled in a three-electrode system (6 mol L^{-1} KOH aqueous solution as the electrolyte). Figure 5a shows the typical cyclic voltammetry (CV) curves of the samples at 5 mV s^{-1}. The curves demonstrate a quasi-rectangular shape with slight distortion, which is induced by the pseudocapacitance with the presence of oxygen-containing functional groups. In comparison with the neat RGO aerogels and neat C-fabrics, the binary 3D architectures (RGO fabrics) apparently have a much larger area (Figure 5a), indicating enhanced energy-storage capability. As exhibited in Figure 5b, the galvanostatic charge−discharge curves of the samples (at current density of 0.6 A g^{-1}) and the almost isosceles triangles illustrate typical double-layer

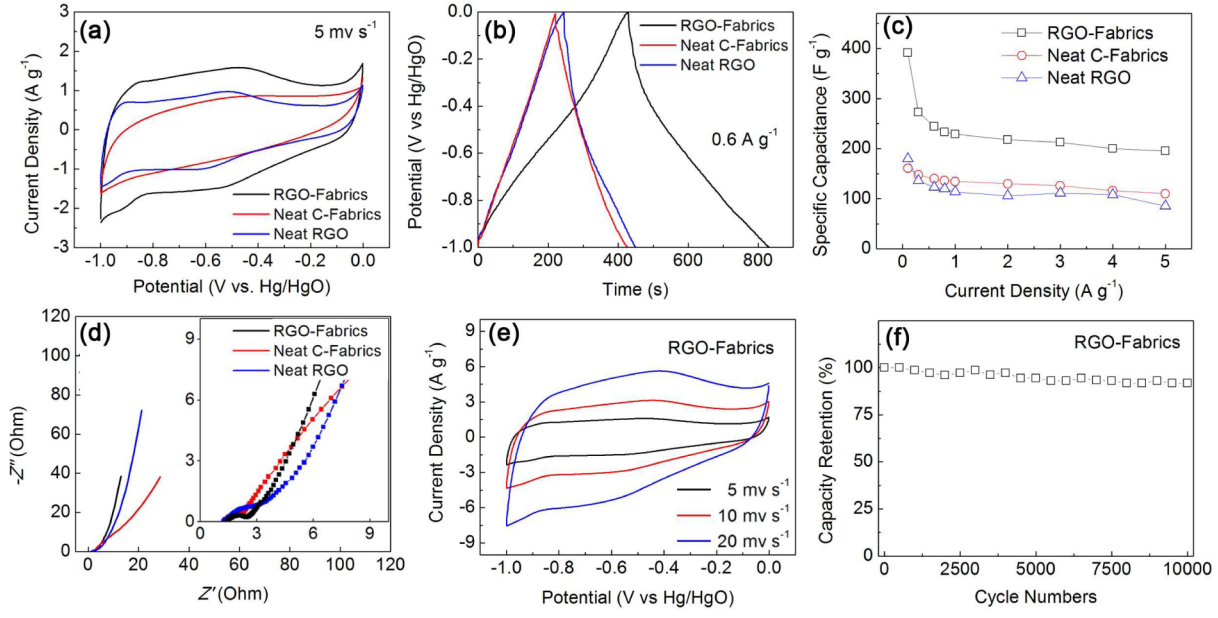

Figure 5. CV curves of the samples as marked (a); typical galvanostatic charge−discharge curves of the samples at current density of 0.6 A g^{-1} (b); specific capacitance of the samples at different current densities (c); Nyquist plots for the samples at a direct current bias of 0 V with a sinusoidal signal of 10 mV over the frequency range 100 kHz to 0.01 Hz (d); CV curves of the RGO fabrics at different scanning rates (e); Cycling stability of the RGO fabrics in the three-electrode system (f).

DOI: 10.1021/am508624x
ACS Appl. Mater. Interfaces 2015, 7, 4257−4264

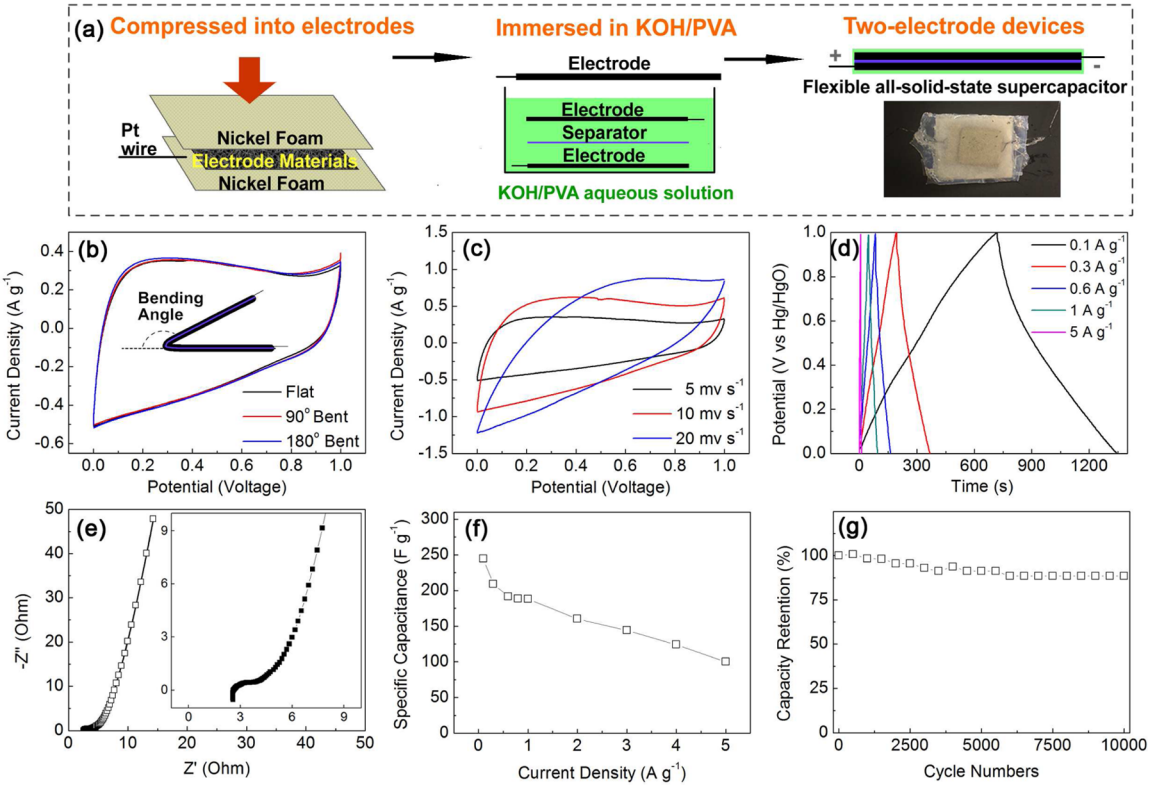

Figure 6. Fabrication of flexible all-solid-state devices based on RGO fabrics (a); CV curves of the flexible device at different bending angles (b); CV curves of the flexible device at different scanning rates (c); typical galvanostatic charge−discharge curves of the flexible device at different current densities (d); Nyquist plots for the flexible device (e); specific capacitance of the flexible device at different current densities (f); cycling stability of the flexible device (g).

capacitance with no obvious voltage drop (IR drop). Therefore, the results also suggest that the employment of C-fabrics in the RGO aerogels enables the RGO fabrics to present improved specific capacitance. As plotted in Figure 5c, the specific capacities at different current densities demonstrate that the RGO fabrics possess the highest capacities, approaching 391, 229, and 195 F g^{-1} at current densities of 0.1, 1, and 5 A g^{-1}, respectively. These values were observed to be substantially higher than those in both of the neat C-fabrics and neat RGO aerogels (Figure 5c). Consequently, such considerable enhancement in the energy storage should be associated with the synergy effects based on the binary 3D architectures.

For fundamentally understanding the mechanisms in the impact of binary 3D architectures on the charge transport/diffusion, electrochemical impedance spectroscopy (EIS) in Figure 5d shows the typical Nyquist plots of the samples. Accordingly, the Nyquist plots were further fitted with the equivalent circuit (Supporting Information, Figure S4) by the model in the previous work,[45,46] and the corresponding fitted parameters were listed in Supporting Information, Table S3. At higher frequency (>10 kHz), the intersection points on the real axis, which is mainly associated with ohmic resistance of the electrolyte and internal resistance of the electrode,[45,46] exhibit very similar values at ∼1.2−1.4 Ohm for all three samples, which is in good agreement with the fitted parameter R_s in Table S3. In the range from high- to midfrequency, the semicircular curves, referring to the interfacial charge transfer resistance (R_{CT}) and double-layer capacitance (C_{DL}),[45,46] indicate that the values were estimated to be 0.9, 1.2, and 2.0 Ohm for the neat C-fabrics, RGO fabrics, and neat RGO, respectively (Figure 5d). At the lower frequency, the long tails in the Nyquist plots demonstrate that the RGO fabrics possess the highest slope, indicating the optimized polarizable capacitance among the three samples. Thes EIS results suggest that, although the impedance of the RGO fabrics has been slightly increased due to the residual oxygen-containing functional groups in the RGO (Figure 3), much improved ionic transport for the formation of electrical double layers has been achieved via the establishment of binary 3D architectures (Table S3).

As shown in Figure 5e, CV curves for the RGO-fabric electrode at different scanning rates were separately exhibited, presenting enlarged area with increasing scanning rate as expected. Such electrode was further applied to 10,000 cycles at the current density of 3 A g^{-1}, which shows excellent cycling stability (retention up to 92% after cycles).

The binary 3D architectures were further processed into a symmetrical two-electrode system to fabricate a flexible all-solid-state supercapacitor. In a preparation of the flexible devices (Figure 6a), a single electrode was initially fabricated by compressing the electrode materials into two pieces of nickel foams. Two as-prepared electrodes with a separator in between were stacked and further immersed into a PVA aqueous solution, followed by adding KOH aqueous solution. The PVA-based gel settled for 2 d, allowing them to form a robust flexible all-solid-state device (Figure 6a). Figure 6b illustrates the CV curves of the flexible device under bending conditions, and no significant change was observed at different bending angles, indicating excellent capacitance retention upon external stress. As shown in Figure 6c, CV curves present a typical double-layer capacitive behavior at different current densities, and redox peaks associated with functional groups have been slightly

DOI: 10.1021/am508624x
ACS Appl. Mater. Interfaces 2015, 7, 4257−4264

suppressed. According to the galvanostatic charge/discharge curves in Figure 6d, similar isosceles triangles at different current densities were also observed. In the two-electrode system, the specific capacitance was calculated by the equation of $C_s = 4I \times t/V/m$, where m is the mass of the total active material of the two electrodes. In Figure 6e, the electrochemical impedance spectroscopy shows only slightly increased impedance (~1.8 Ohm) in the flexible all-solid-state supercapacitor, compared to the values found in the three-electrode system. The vertical line in the low-frequency region also indicates the fast ionic transport in the solid-state PVA/KOH electrolyte (Figure 6e). Plotted in Figure 6f is the specific capacitance at different current densities, suggesting the highest capacity up to 245 F g^{-1} at 0.1 A g^{-1}. Additionally, the all-solid-state supercapacitor also presented good cycling stability with 90% retention after 10 000 cycles at a current density of 2 A g^{-1} (Figure 6g).

As aforementioned, comparison of Figures 5e and 6c suggests that the distorted rectangular shape induced by the pseudocapacitance (associated with oxygen-containing functional groups) in the three-electrode system has been suppressed in the two-electrode system. Such suppression has also been found in the other similar solid KOH/PVA-based two-electrode systems,[27] but the mechanism is still not clear. Probably, the hydrogen bonding between the alcohol groups in PVA and oxygen-containing functional groups in the carbon materials might reduce the pseudocapacitive interaction in the basic all-solid-state capacitors. Apparently, the related mechanism requires more specific investigations in the near future.

Specific capacitance of the recently reported graphene-based and aerogel-like structures in the three-electrode and two-electrode systems is given in Supporting Information, Tables S4 and S5, respectively. The electrochemical performance of the RGO fabrics in both three-electrode and two-electrode systems competes well and is even higher than that of some typical graphene-based nanostructures (Tables S4 and S5). Moreover, the Ragone chart of the all-solid-state supercapacitors suggests that the performance of the RGO fabrics here is also competitive to or even larger than some typical graphene-based nanostructures (Supporting Information, Figure S5). According to the above comparison, the strategy in this work obviously indicates room for more improvement, including modifying the GO quality and concentration, tuning the porous structures, and optimizing the channels and impedance for ionic and electronic transport, whereby advanced carbon-based energy-storage devices may be achieved. Nonetheless, the synergy effects by using C-fabrics to engineer the interface, nanostructure, and electrochemical performance of the RGO aerogels have suggested a highly promising way to design and optimize the carbon-based energy-storage electrodes and devices. More importantly, in the traditional methods of introducing carbon spacers[25−27,29,30] into the graphene-based aerogels, the 3D graphene frameworks are known to play the crucial role in the formation of the main skeletons, whose mechanical stability might be diminished due to the introduced spacers.[27] However, in this work, the mechanical stability of the resulting binary 3D porous architectures is dominantly determined by the robust C-fabrics (Figure 2), and thus related concerns could be completely avoided. Meanwhile, associated issues can be further improved by substituting the C-fabrics with other 3D fabrics of specific properties, and thereby the binary 3D architectures with more special performance could be envisaged. As a consequence, the utilization of a 3D skeleton for engineering 3D graphene framework highlights a versatile platform for the facile preparation of novel binary 3D porous architectures. Specifically, such exclusive strategy could be widely applied to many other fields, where robust 3D porous architectures of unique properties are required.

CONCLUSIONS

In summary, we have demonstrated a simple and versatile approach toward fabricating a novel binary 3D porous architecture, where 3D porous carbon fabrics served as the skeleton in the formation of the RGO aerogels. The results indicate that employment of carbon fabrics plays the significant role in engineering the interface, nanostructure, and electrochemical performance of the RGO aerogels. The fundamental mechanisms for the enhancement in the energy storage suggest that the strategy for interfacial engineering has promised a unique platform to substantially improve interfaces and related transport properties in various 3D porous structures, showing great application potential in many fields.

EXPERIMENTAL SECTION

Chemicals. Graphite powder was supplied by Sigma-Aldrich. Concentrated sulfuric acid (H_2SO_4, 98%), nitric acid (HNO_3, 70%), sodium nitrate ($NaNO_3$, AR), potassium permanganate ($KMnO_4$, AR), hydrogen peroxide (H_2O_2, 38%), hydrochloric acid (HCl, 38%), ethanol (AR), hydroquinone (AR), and poly(vinyl alcohol) (PVA, M_w: > 80 000, hydrolyzed) were purchased from Beijing Chemicals Co. Ltd. C-fabrics of large surface area (~1111 m^2 g^{-1}) were commercially provided by Fanghua Institute (parameters and feature available in the text).

Graphene Oxide. GO was prepared according to the modified Hummers method.[47] In brief, commercial graphite (2 g) and $NaNO_3$ powders (1 g) were added into concentrated H_2SO_4 (120 Ml) in an ice bath and the mixture was kept at 0 °C for 1 h, followed by adding $KMnO_4$ (6 g) gradually (*Caution*: must be slowly added.). After stirring for 2h, the mixture was heated and kept at 30 °C for 0.5 h. Subsequently, water (150 mL) was dropwise added, followed by adding H_2O_2 (5%, 50 mL). Finally, the solution was washed with water and HCl (5%) to obtain the GO aqueous solution.

RGO-Fabric Binary Three-Dimensional Architectures. In the typical preparation of RGO fabrics, C-fabrics were first treated in the solution of H_2SO_4 and HNO_3 (vol/vol = 3:1) under sonication for 1 h to improve the hydrophilicity. A piece of the acid-treated C-fabrics was positioned in the GO aqueous solution (5 mg/mL) under sonication for 2 h, followed by adding hydroquinone with a mass ratio of 1:5 (GO/hydroquinone). Until a stable solution was achieved, the extra solution above the C-fabrics was carefully removed, and the remaining mixture was sealed in a box. Subsequently, the sealed box was heated to 100 °C for 12 h in a vacuum oven, allowing GO to be in situ self-assembled into hydrogels. After the oven was cooled to room temperature, the product was washed with water and then immersed in 1 L water for 2 d to remove the chemical residues. The sample was further freeze-dried to achieve aerogel-like dried product, and it was thermally annealed at 300 °C for 1 h with the protection of nitrogen atmosphere. The mass ratio of the C-fabrics to RGO was estimated to be 16:3 prior to 300 °C thermal annealing. In the thermal annealing at 300 °C, the mass retention for the neat RGO and acid-treated C-fabrics was estimated to be 92.6% and 86%, respectively. Hence, the mass loading of the C-fabrics in the resulting RGO fabrics was estimated to be ~85%. For the reference samples, neat RGO aerogels were prepared with the same conditions expect for the use of C-fabrics.

Characterizations. Field-emission SEM was conducted on ZEISS supra 55 system, and TEM was performed on JEOL JEM-2010. The nitrogen absorption/desorption isotherms associated with specific surface area and pore diameter distribution data were investigated on an Autosorb-iQ2-MP (Quantachrome) analyzer under 77 K. XPS

DOI: 10.1021/am508624x
ACS Appl. Mater. Interfaces 2015, 7, 4257−4264

spectra were acquired on PHI-5300 system. Raman spectrum was obtained on HR800 (Horiba JobinYvon) with a 514.5 nm Ar-ion laser.

Electrochemical Characterizations (Three-Electrode System). The electrochemical performance of the samples was determined in a three-electrode system with basic aqueous solutions. The working electrode was prepared by mixing the samples, acetylene black with poly(tetrafluoroethylene) in a mass ratio of 80:15:5, and then the mixture was pressed onto a piece of nickel foam. The typical mass and dimensions of the working electrodes are 5 mg and 1 cm^2. For the three-electrode system, Pt and Hg/HgO electrodes were used as the counter electrode and reference electrode, respectively, while the KOH solution (6 mol L^{-1}) was employed as the electrolyte. Galvanostatic charge/discharge was tested at various current densities using LAND-CT2001A (Wuhan Jinnuo Electronics. Ltd.). CV and EIS were carried out using a CHI660C electrochemical workstation (CH Instruments, Inc.).

Electrochemical Characterizations (Two-Electrode Devices). The electrochemical performance of the RGO fabrics was further determined in an all-solid-state two-electrode device. In a typical preparation of the electrode (Figure 6a), the electrode materials were directly compressed into two pieces of nickel foams under the pressure of 10 MPa. The electrode was connected to a Pt wire to form the working electrode. In a preparation of the flexible devices, PVA powder (2 g) was initially dissolved in the distilled water (20 mL) under vigorous stirring at 85 °C. Until a stable PVA aqueous solution was formed, two working electrodes with a separator in between were stacked and further immersed into PVA aqueous solution, followed by adding excess KOH aqueous solution (6 mol L^{-1}). The PVA-based gel settled for 2 d, allowing it to form a robust flexible all-solid-state device (Figure 6a). In the bending test, the flexible device was bent to different angles, while the CV curves were recorded. The specific capacitance was calculated according to the equation of $C_s = I \times t/V/m$, where C_s (F g^{-1}) is the specific capacity, I (A g^{-1}) is the response current density, t (s) is the discharge time, V (V) is the potential, and m (g) is the mass of active material. The specific energy density (E) and power density (P) are given as $E = C_s \times V^2/7.2$ (Wh kg^{-1}) and $P = E \times 3600/t$ (W kg^{-1}), respectively.

■ ASSOCIATED CONTENT

Supporting Information

Additional SEM images, Raman spectra, XPS data, Ragone chart, parameters of the specific surface area, fitted values for equivalent circuit of impedance spectra, comparison of electrochemical performance for the graphene-based and aerogel-like nanostructures, and additional references. This material is available free of charge via the Internet at http://pubs.acs.org.

■ AUTHOR INFORMATION

Corresponding Author

*Phone/Fax: +86 10 6233-3548. E-mail: fanlizhen@ustb.edu.cn.

Notes

The authors declare no competing financial interest.

■ ACKNOWLEDGMENTS

Financial support from 973 Project (2013CB934001 and 2015CB932500), NSF of China (51172024, 51372022, and 51302011), China PSF (2014T70037), and the Fundamental Research Funds for the Central Universities (FRF-TP-09-007A and FRF-TP-14-091A2) are gratefully acknowledged.

■ REFERENCES

(1) Miller, J. R.; Simon, P. Electrochemical Capacitors for Energy Management. *Science* **2008**, *321*, 651−652.
(2) Simon, P.; Gogotsi, Y. Materials for Electrochemical Capacitors. *Nat. Mater.* **2008**, *7*, 845−854.
(3) Wang, G. P.; Zhang, L.; Zhang, J. J. A Review of Electrode Materials for Electrochemical Supercapacitors. *Chem. Soc. Rev.* **2012**, *41*, 792−828.
(4) Simon, P.; Gogotsi, Y. Capacitive Energy Storage in Nanostructured Carbon-Electrolyte Systems. *Acc. Chem. Res.* **2013**, *46*, 1094−1103.
(5) Zhai, Y. P.; Dou, Y. Q.; Zhao, D. Y.; Fulvio, P. F.; Mayes, R. T.; Dai, S. Carbon Materials for Chemical Capacitive Energy Storage. *Adv. Mater.* **2011**, *23*, 4828−4850.
(6) Zhao, L.; Fan, L. Z.; Zhou, M. Q.; Guan, H.; Qiao, S. Y.; Antonietti, M.; Titirici, M. M. Nitrogen-Containing Hydrothermal Carbons with Superior Performance in Supercapacitors. *Adv. Mater.* **2010**, *22*, 5202−5206.
(7) El-Kady, M. F.; Strong, V.; Dubin, S.; Kaner, R. B. Laser Scribing of High-Performance and Flexible Graphene-Based Electrochemical Capacitors. *Science* **2012**, *335*, 1326−1330.
(8) Xu, Y.; Lin, X.; Zhong, Z. Y.; Huang, X.; Weiss, X. Q.; Nathan, O.; Duan, X. F. Holey Graphene Frameworks for Highly Efficient Capacitive Energy Storage. *Nat. Commun.* **2014**, *5*, 4554−4561.
(9) Wu, Z. S.; Parvez, K.; Feng, X. L.; Mullen, K. Graphene-Based in-Plane Micro-Supercapacitors with High Power and Energy Densities. *Nat. Commun.* **2013**, *4*, 2487−2494.
(10) Jiang, H.; Lee, P. S.; Li, C. Z. 3D Carbon Based Nanostructures for Advanced Supercapacitors. *Energy Environ. Sci.* **2013**, *6*, 41−53.
(11) Chabi, S.; Peng, C.; Hu, D.; Zhu, Y. Q. Ideal Three-Dimensional Electrode Structures for Electrochemical Energy Storage. *Adv. Mater.* **2014**, *26*, 2440−2445.
(12) Aboutalebi, S. H.; Jalili, R.; Esrafilzadeh, D.; Salari, M.; Gholamvand, Z.; Yamini, S. A.; Konstantinov, K.; Shepherd, R. L.; Chen, J.; Moulton, S. E.; Innis, P. C.; Minett, A. I.; Razal, J. M.; Wallace, G. G. High-Performance Multifunctional Graphene Yarns: Toward Wearable All-Carbon Energy Storage Textiles. *ACS Nano* **2014**, *8*, 2456−2466.
(13) Biener, J.; Stadermann, M.; Suss, M.; Worsley, M. A.; Biener, M. M.; Rose, K. A.; Baumann, T. F. Advanced Carbon Aerogels for Energy Applications. *Energy Environ. Sci.* **2011**, *4*, 656−667.
(14) Nardecchia, S.; Carriazo, D.; Ferrer, M. L.; Gutierrez, M. C.; Monte, F. D. Three Dimensional Macroporous Architectures and Aerogels Built of Carbon Nanotubes and/or Graphene: Synthesis and Applications. *Chem. Soc. Rev.* **2013**, *42*, 794−830.
(15) Worsley, M. A.; Pauzauskie, P. J.; Olson, T. Y.; Biener, J.; Satcher, J. H., Jr.; Baumann, T. F. Synthesis of Graphene Aerogel with High Electrical Conductivity. *J. Am. Chem. Soc.* **2010**, *132*, 14067−14069.
(16) Xu, Y. X.; Lin, Z. Y.; Huang, X. Q.; Liu, Y.; Huang, Y.; Duan, X. F. Flexible Solid-State Supercapacitors Based on Three-Dimensional Graphene Hydrogel Films. *ACS Nano* **2013**, *7*, 4042−4049.
(17) Lin, Y.; Ehlert, G. J.; Bukowaky, C.; Sodano, H. A. Superhydrophobic Functionalized Graphene Aerogel. *ACS Appl. Mater. Interfaces* **2011**, *3*, 2200−2203.
(18) Wang, Z. L.; Xu, D.; Wang, H. G.; Wu, Z.; Zhang, X. B. In Situ Fabrication of Porous Graphene Electrodes for High-Performance Energy Storage. *ACS Nano* **2013**, *7*, 2422−2430.
(19) Wang, X. B.; Zhang, Y. J.; Zhi, C. Y.; Wang, X.; Tang, D. M.; Xu, Y. B.; Weng, Q. H.; Jiang, X. F.; Mitome, M.; Golberg, D.; Bando, Y. Three-Dimensional Strutted Graphene Grown by Substrate-Free Sugar Blowing for High-Power-Density Supercapacitors. *Nat. Commun.* **2013**, *4*, 2905−2912.
(20) Xu, Y. X.; Lin, Z. Y.; Huang, X. Q.; Wang, Y.; Huang, Y.; Duan, X. F. Functionalized Graphene Hydrogels Based High-Performance Supercapacitors. *Adv. Mater.* **2013**, *25*, 5779−5784.
(21) Cao, X. H.; Yin, Z. Y.; Zhang, H. Three-Dimensional Graphene Materials: Preparation, Structures and Application in Supercapacitors. *Energy Environ. Sci.* **2014**, *7*, 1850−1865.
(22) Wu, Z. S.; Winter, A.; Chen, L.; Sun, Y.; Turchanin, A.; Feng, X.; Müllen, K. Three-Dimensional Nitrogen and Boron Co-doped

DOI: 10.1021/am508624x
ACS Appl. Mater. Interfaces 2015, 7, 4257−4264

Graphene for High-Performance All-Solid-State Supercapacitors. *Adv. Mater.* **2012**, *24*, 5130−5135.
(23) Zhao, Y.; Hu, C. G.; Hu, Y.; Cheng, H. H.; Shi, G. Q.; Qu, L. T. A Versatile, Ultralight, Nitrogen-Doped Graphene Framework. *Angew. Chem., Int. Ed.* **2012**, *124*, 11533−11537.
(24) You, B.; Wang, L. L.; Yao, L.; Yang, J. Three Dimensional N-doped Graphene−CNT Networks for Supercapacitor. *Chem. Commun.* **2013**, *49*, 5016−5018.
(25) Chen, W. C.; Li, S.; Chen, C. H.; Yan, L. F. Self-Assembly and Embedding of Nanoparticles by in situ Reduced Graphene for Preparation of a 3D Graphene/Nanoparticle Aerogel. *Adv. Mater.* **2011**, *23*, 5679−5683.
(26) Wang, G. K.; Sun, X.; Lu, F. Y.; Sun, H. T.; Yu, M. P.; Jiang, W. L.; Liu, C. S.; Lian, J. Flexible Pillared Graphene-Paper Electrodes for High-Performance Electrochemical Supercapacitors. *Small* **2012**, *8*, 452−459.
(27) Ju, H. F.; Song, W. L.; Fan, L. Z. Rational Design of Graphene/Porous Carbon Aerogels for High-Performance Flexible All-Solid State Supercapacitors. *J. Mater. Chem. A* **2014**, *2*, 10895−10903.
(28) Dong, X. C.; Xu, H.; Wang, X. W.; Huang, Y. X.; Chan-Park, M. B.; Zhang, H.; Wang, Y. X.; Huang, W.; Chen, P. 3D Graphene−Cobalt Oxide Electrode for High-Performance Supercapacitor and Enzymeless Glucose Detection. *ACS Nano* **2012**, *6*, 3206−3213.
(29) Wang, Y.; Wu, Y. P.; Huang, Y.; Zhang, F.; Yang, X.; Ma, Y. F.; Chen, Y. S. Preventing Graphene Sheets from Restacking for High-Capacitance Performance. *J. Phys. Chem. C* **2011**, *115*, 23192−23197.
(30) Sui, Z. Y.; Meng, Q. H.; Zhang, X. T.; Ma, R.; Cao, B. Green Synthesis of Carbon Nanotube−Graphene Hybrid Aerogels and Their Use as Versatile Agents for Water Purification. *J. Mater. Chem.* **2012**, *22*, 8767−8771.
(31) Yang, P. H.; Ding, Y.; Chen, Z. W.; Li, Y. Z.; Qiang, P. F.; Ebrahimi, M.; Mai, W. J.; Wong, C. P.; Wang, Z. L. Low-Cost High-Performance Solid-State Asymmetric Supercapacitors Based on MnO_2 Nanowires and Fe_2O_3 Nanotubes. *Nano Lett.* **2014**, *14*, 731−736.
(32) Liu, B.; Zhang, J.; Wang, X. F.; Chen, G.; Chen, D.; Zhou, C. W.; Shen, G. Z. Hierarchical Three-Dimensional $ZnCo_2O_4$ Nanowire Arrays/carbon Cloth Anodes for a Novel Class of High-Performance Flexible Lithium-Ion Batteries. *Nano Lett.* **2012**, *12*, 3005−3011.
(33) Hsu, Y. K.; Chen, Y. C.; Lin, Y. G.; Chen, L. C.; Chen, K. H. High-Cell-Voltage Supercapacitor of Carbon Nanotube/Carbon Cloth Operating in Neutral Aqueous Solution. *J. Mater. Chem.* **2012**, *22*, 3383−3387.
(34) Ren, W.; Wang, C.; Lu, L. F.; Li, D. D.; Cheng, C. W.; Liu, J. P. SnO_2@Si Core−Shell Nanowire Arrays on Carbon Cloth as a Flexible Anode for Li Ion Batteries. *J. Mater. Chem. A* **2013**, *1*, 13433−13438.
(35) Xiong, Q. Q.; Tu, J. P.; Xia, X. H.; Zhao, X. Y.; Gu, C. D.; Wang, X. L. A Three-Dimensional Hierarchical Fe_2O_3@NiO Core/Shell Nanorod Array on Carbon Cloth: A New Class of Anode for High-Performance Lithium-Ion Batteries. *Nanoscale* **2013**, *5*, 7906−7912.
(36) Yang, W. L.; Gao, Z.; Ma, J.; Zhang, X. M.; Wang, J.; Liu, J. Y. Hierarchical $NiCo_2O_4$@NiO Core−Shell Hetero-Structured Nanowire Arrays on Carbon Cloth for a High-Performance Flexible All-Solid-State Electrochemical Capacitor. *J. Mater. Chem. A* **2014**, *2*, 1448−1457.
(37) Xu, Y. X.; Sheng, K. X.; Li, C.; Shi, G. Q. Self-Assembled Graphene Hydrogel via a One-Step Hydrothermal Process. *ACS Nano* **2010**, *4*, 4324−4330.
(38) Stankovich, S.; Dikin, D. A.; Piner, R. D.; Kohlhaas, K. A.; Kleinhammes, A.; Jia, Y.; Wu, Y.; Nguyen, S. T.; Ruoff, R. S. Synthesis of Graphene-Based Nanosheets via Chemical Reduction of Exfoliated Graphite Oxide. *Carbon* **2007**, *45*, 1558−1565.
(39) Fan, L. Z.; Qiao, S. Y.; Song, W. L.; Wu, M.; He, X. B.; Qu, X. H. Effects of the Functional Groups on the Electrochemical Properties of Ordered Porous Carbon for Supercapacitors. *Electrochim. Acta* **2013**, *105*, 299−304.
(40) Fan, L. Z.; Liu, J. L.; Ud-Din, R.; Yan, X. Q.; Qu, X. H. The Effect of Reduction Time on the Surface Functional Groups and Supercapacitive Performance of Graphene Nanosheets. *Carbon* **2012**, *50*, 3724−3730.
(41) Sun, L.; Wang, L.; Tian, C. G.; Tan, T. X.; Xie, Y.; Shi, K. Y.; Li, M. T.; Fu, H. G. Nitrogen-Doped Graphene with High Nitrogen Level via a One-Step Hydrothermal Reaction of Graphene Oxide with Urea for Superior Capacitive Energy Storage. *RSC Adv.* **2012**, *2*, 4498−4506.
(42) Lee, K. H.; Oh, J.; Son, J. G.; Kim, H.; Lee, S. S. Nitrogen-Doped Graphene Nanosheets from Bulk Graphite Using Microwave Irradiation. *ACS Appl. Mater. Interfaces* **2014**, *6*, 6361−6368.
(43) Kruk, M.; Jaroniec, M. Gas Adsorption Characterization of Ordered Organic−Inorganic Nanocomposite Materials. *Chem. Mater.* **2001**, *13*, 3169−3183.
(44) Zhang, L. L.; Zhao, X.; Stoller, M. D.; Zhu, Y. W.; Ji, H. X.; Murali, S.; Wu, Y. P.; Perales, S.; Clevenger, B.; Ruoff, R. S. Highly Conductive and Porous Activated Reduced Graphene Oxide Films for High-Power Supercapacitors. *Nano Lett.* **2012**, *12*, 1806−1812.
(45) Choi, B. G.; Hong, J.; Hong, W. H.; Hammond, P. T.; Park, H. Facilitated Ion Transport in All-Solid-State Flexible Supercapacitors. *ACS Nano* **2011**, *5*, 7205−7213.
(46) Masarapu, C.; Zeng, H. F.; Hung, K. H.; Wei, B. Q. Effect of Temperature on the Capacitance of Carbon Nanotube Supercapacitors. *ACS Nano* **2009**, *3*, 2199−2206.
(47) Hummers, W.; Fleman, R. O. Preparation of Graphitic Oxide. *J. Am. Chem. Soc.* **1958**, *80*, 1339.

DOI: 10.1021/am508624x
ACS Appl. Mater. Interfaces 2015, 7, 4257−4264